

1 **Multi-Machine Learning Ensemble Regionalization of Hydrological  
2 Parameters for Enhancing Flood Prediction in Ungauged  
3 Mountainous Catchments**

4  
5 Kai Li, Linmao Guo, Genxu Wang\*, Jihui Gao\*, Xiangyang Sun, Peng Huang,  
6 Jinlong Li, Jiapei Ma, Xinyu Zhang

7  
8 *State Key Laboratory of Hydraulics and Mountain River Engineering, College of Water Resource  
9 and Hydropower, Sichuan University, Chengdu, 610000, China*

10 \*Corresponding author: Genxu Wang (wanggx@scu.edu.cn) and Jihui Gao (jgao@scu.edu.cn).

11

12 **Abstract:**

13 Machine learning-based parameter regionalization is an important method for  
14 flood prediction in ungauged mountainous catchments. However, single machine  
15 learning parameter regionalization often exhibits limitations in prediction accuracy and  
16 robustness. Therefore, this study proposes a multi-machine learning ensemble  
17 regionalization method that integrates Gradient Boosting Machine (GBM), K-Nearest  
18 Neighbors (KNN), and Extremely Randomized Trees (ERT) methods (GBM-KNN-  
19 ERT) to regionalize the sensitive parameters of the Topography-Based Subsurface  
20 Storm Flow (Top-SSF) model. Validated across 80 mountainous catchments in  
21 southwestern China, the GBM-KNN-ERT method demonstrates superior performance  
22 with 90% of ungauged catchments achieving the Nash-Sutcliffe Efficiency (NSE)  
23 above 0.9, representing a 67.44% improvement over the best single machine learning  
24 parameter regionalization. Notably, the GBM-KNN-ERT method shows improved  
25 robustness to climate change and changes in the number of donor catchments compared  
26 to other regionalization methods. An optimal balance between accuracy and

27 computational efficiency was achieved using 20-40 high quality donor catchments  
28 (NSE greater than 0.85). This study provides systematic evidence that multi-machine  
29 learning ensemble can effectively address regionalization challenges in ungauged  
30 mountainous regions, offering a reliable tool for water resource management and flood  
31 disaster mitigation.

32 **Keywords:** Flood forecasting; Regionalization; Ungauged mountainous catchments;  
33 Top-SSF model;

34

35 **Highlights:**

36 1. Proposes a novel multi-machine learning ensemble regionalization method  
37 2. The GBM-KNN-ERT method increases the percentage of catchments with high-  
38 accuracy flood predictions (NSE >0.9) to 90%, which is a 67.44% improvement  
39 over the best single ML method.

批注 [L1]: RC2 Comment#2

40 3. The GBM-KNN-ERT method exhibits greater stability under climate change.  
41

42      **1. Introduction**

43      **Floods in mountainous catchments, encompassing both flash floods and general**  
44      **larger-scale flood events which can be derived from mountainous upland catchments,**  
45      **pose a significant threat to human safety and property, particularly in regions lacking**  
46      **sufficient observational data** (Luo et al., 2015; Zhai et al., 2018). While hydrological  
47      models like the Topography-Based Subsurface Storm Flow (Top-SSF) model (Li et al.,  
48      2024) offer promising simulation capabilities, their application in ungauged catchments  
49      is severely limited by the absence of calibration data (Choi et al., 2023; Liu et al., 2018).  
50      Effective parameter regionalization methods are therefore essential for transferring  
51      hydrological knowledge from gauged to ungauged regions, enabling reliable flood  
52      prediction in ungauged mountainous catchment (Garambois et al., 2015; Ragettli et al.,  
53      2017; Xu et al., 2018).

批注 [L2]: RC2, omment#5

54      Parameter regionalization is a crucial method for flood prediction in ungauged  
55      catchments (Arsenault et al., 2022; Guo et al., 2021; Kratzert et al., 2019; Zhang et al.,  
56      2020). Compared to purely data-driven methods, parameter regionalization offers  
57      enhanced physical interpretability (Nearing et al., 2024; Tang et al., 2023; Zhang et al.,  
58      2024). Existing parameter regionalization methods can be broadly classified into three  
59      categories: similarity-based, hydrological signatures-based, and regression-based  
60      (Arsenault et al., 2019; Wu et al., 2022). Similarity-based methods rely on the  
61      assumption that catchments with similar characteristics exhibit similar hydrological  
62      responses, considering spatial proximity (Arsenault et al., 2019; Pugliese et al., 2018;  
63      Yang et al., 2018) and physical similarity (similar climatic and land cover conditions

64 have similar hydrological characteristics) (Kanishka et al., 2017; Papageorgaki et al.,  
65 2016). Hydrological signature-based methods use hydrological signatures (quantitative  
66 metrics that describe statistical or dynamic properties of streamflow) as an intermediate  
67 link, establishing relationships first between model parameters and signatures, and then  
68 between signatures and catchment descriptors to facilitate parameter transfer  
69 (McMillan, 2021; Zhang et al., 2018). Regression-based methods, which directly link  
70 hydrological model parameters to catchment descriptors, are widely used due to their  
71 simplicity and computational efficiency (Guo et al., 2021; Kratzert et al., 2019; Song et  
72 al., 2022; Wu et al., 2022). However, the performance of regression-based methods is  
73 frequently constrained by the inherent nonlinearity in the relationships between model  
74 parameters and catchment descriptors, coupled with the difficulty in adequately  
75 capturing spatial heterogeneity, especially within complex mountainous terrain (Wu et  
76 al., 2022).

77 Recent advances in machine learning offer potential solutions by capturing  
78 nonlinear patterns in high-dimensional data. Such as Decision Tree (DT), Extremely  
79 Randomized Trees (ERT), Gradient Boosting Machine (GBM), K-Nearest Neighbor  
80 (KNN), Random Forest (RF), and Support Vector Machines (SVM) have shown  
81 promise in parameter regionalization (Golian et al., 2021; Song et al., 2022). However,  
82 existing machine learning-based parameter regionalization studies predominantly focus  
83 on runoff prediction at coarser temporal scales (daily or monthly) (Li et al., 2022; Wu  
84 et al., 2022), leaving a significant gap in high-resolution (hourly or sub-hourly) flood  
85 prediction in ungauged mountainous catchments. Moreover, these studies often rely on

86 single machine learning methods to estimate all hydrological model parameters (Golian  
87 et al., 2021; Song et al., 2022; Wu et al., 2022). Given that different machine learning  
88 methods operate on distinct principles (Jordan et al., 2015; Zounemat-Kermani et al.,  
89 2021) and hydrological model parameters represent diverse hydrological processes (Li  
90 et al., 2024), a single machine learning method may not adequately capture the  
91 complexity of model parameter estimation (Golian et al., 2021; Wu et al., 2022).  
92 Therefore, exploring the multi-machine learning ensemble methods is essential to  
93 improve the accuracy of high-resolution flood prediction in ungauged mountainous  
94 catchments.

95 Southwest China's mountainous regions are particularly vulnerable to frequent  
96 floods, leading to ecosystem degradation through habitat disruption and biodiversity  
97 loss (Gan et al., 2018). The abundance of ungauged catchments in this region poses a  
98 significant challenge to reliable flood prediction. To address this critical issue, we  
99 systematically evaluate the performance of a novel multi-machine learning ensemble  
100 method for regionalizing Top-SSF model parameters across 80 representative  
101 catchments (mean area: 1,586 km<sup>2</sup>) in Southwest China. By assessing ensemble method  
102 robustness under climate change and with varying donor catchment configurations, this  
103 study aims to significantly enhance flood prediction accuracy in ungauged mountainous  
104 catchments, contributing to improved ecosystem resilience, enhanced human safety,  
105 and more effective water resource management in the face of escalating climatic  
106 pressures.

107 **2. Study area and datasets**

108 **2.1. Study area**

109 This study investigated 80 mountainous catchments in Southwestern China,  
110 encompassing Sichuan, Yunnan, Guangxi, Guizhou, and Chongqing provinces (Fig. 1).

111 This region exhibits diverse climatic zones, including subtropical monsoon, plateau  
112 mountain, and tropical monsoon climates. The selected catchments have an average  
113 area of 1,586 km<sup>2</sup> (ranging from 109 to 6,564 km<sup>2</sup>), with elevations ranging from 63 to

批注 [L3]: RC1, Comment#1

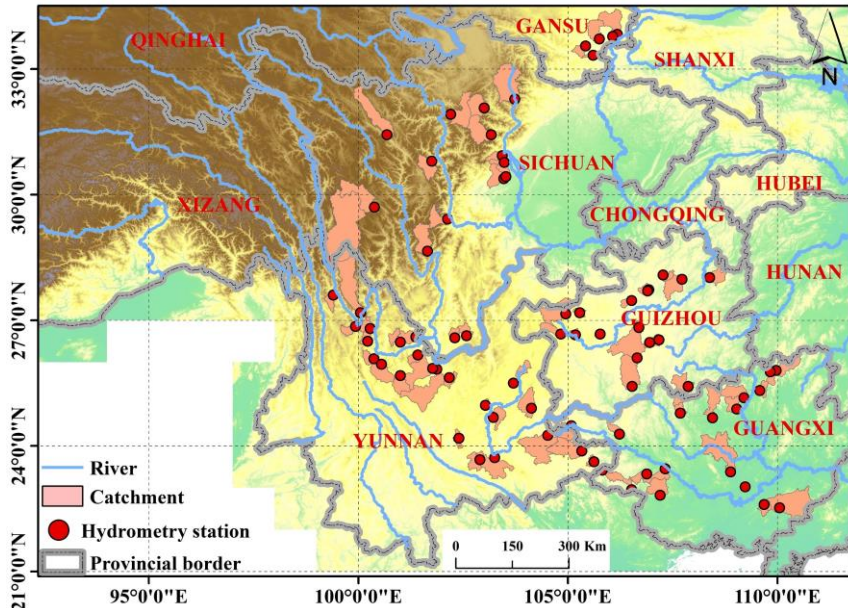
114 6,284 meters. Mean annual temperature varies from 15 to 20°C, and annual  
115 precipitation ranges from 1,200 to 1,800 mm (Li et al., 2016), with approximately 80%  
116 of the annual precipitation occurring during summer and autumn, contributing to  
117 frequent flooding events (Cheng et al., 2019). These catchments are situated within a  
118 heavily forested region, the second largest in China (Hua et al., 2018), with forest cover  
119 ranging from 3% to 92% (mean: 51%), influencing evapotranspiration and runoff

120 generation. Dominant soil types, according to the Genetic Soil Classification of China

121 (Shi et al., 2004), include purple soil (12.20%), yellow soil (11.39%), and red soil

122 (9.52%), each with distinct hydrological properties.

批注 [L4]: RC2, Comment#6



123 **Fig.1.** Geographical distribution of the 80 gauged catchments used, with locations of  
 124 hydrometry station (red points) and major rivers indicated.

125 **2.2. Datasets**

126 Hourly flow data (2015–2018) for 80 mountainous catchments in China were

批注 [L5]: RC1, Comment# 2  
RC2, Comment# 7

批注 [L6]: RC1, Comment# 3

127 sourced from the Hydrological Bureau of the Ministry of Water Resources, through

批注 [L7]: RC2, Comment#6

128 China's hydrologic yearbooks, encompassing a spectrum of events from flash floods

129 and general floods which can be derived from mountainous upland catchments. Hourly

130 rainfall data (2015–2018) were obtained from ground meteorological stations across

131 China (<http://en.weather.com.cn>), providing crucial input for hydrological modelling.

132 Additional meteorological variables, including temperature, wind speed, dewpoint

133 temperature, and surface net solar radiation, were obtained from the ERA5 hourly

134 dataset (1940–present) (Hersbach et al., 2023), ensuring comprehensive atmospheric

135 forcing. Relative humidity was estimated using dewpoint temperature. Historical

137 (1901–2021) and projected future (SSP585, 2022–2100) temperature and precipitation  
138 data for China, averaged from the EC-Earth3, GFDL-ESM4, and MRI-ESM2-0 models  
139 at 1 km resolution, were obtained from "A Big Earth Data Platform for Three Poles" to  
140 assess the impact of climate change (Ding et al., 2020) (<http://poles.tpdc.ac.cn>).  
141 Topographic data, including a 30-m resolution Digital Elevation Model (DEM), used  
142 for river network and topographic index derivation, were obtained from EARTHDATA  
143 and used for river network delineation and topographic index derivation  
144 (<https://search.earthdata.nasa.gov/search>). Forest cover data (30-m resolution) were  
145 sourced from the Global Forest Cover and Forest Change Map  
146 (<https://www.noda.ac.cn/>), providing information on vegetation characteristics. Bulk  
147 density (BD) data were derived from the Soil Database of China for Land Surface  
148 Modelling (Dai et al., 2013). Soil hydraulic parameters, specifically saturated hydraulic  
149 conductivity (Ks\_CH) for Clapp and Hornberger functions and the pore-connectivity  
150 parameter (L) for van Genuchten and Mualem functions, were acquired from the China  
151 Dataset of Soil Hydraulic Parameters Using Pedotransfer Functions for Land Surface  
152 Modeling (Shangguan et al., 2013).

153

154

155

156

157

158

159 **Table 1.** Model forcing data and catchment descriptors information.

Data type	Name	Unit	Function
Hydro-meteorology	Rainfall	mm	Input for hydrological model
	Flood	m <sup>3</sup> /s	Used for model calibration (hourly resolution)
	Temperature	K	
	Surface pressure	Pa	
	Dewpoint temperature	K	
	wind speed	m/s	Input for hydrological model
	Surface net solar radiation	J/m <sup>2</sup>	
Soil characteristics	Relative humidity	%	
	1 km monthly precipitation (1901-2021)	mm	
	1 km monthly temperature (1901-2021)	°C	
	1 km monthly temperature (2022-2100, SSP5-8.5, EC-Earth3, GFDL-ESM4, MRI-ESM2-0)	°C	Multi-year surface average as catchment descriptors
	1 km monthly precipitation (2022-2100, SSP5-8.5, EC-Earth3, GFDL-ESM4, MRI-ESM2-0)	mm	
	Soil bulk density (BD)	g/cm <sup>3</sup>	
	Pore-connectivity parameter (L) for the van Genuchten and Mualem functions	-	
Topography	Saturated hydraulic conductivity (K <sub>s</sub> _CH) of the Clapp and Hornberger Functions	cm d <sup>-1</sup>	
	Forest cover (FC)	%	Surface average as catchment descriptors
	DEM	m	
	Topographic index	-	
	Slope	mm <sup>-1</sup>	
	Catchment area	km <sup>2</sup>	

160 

### 3. Methodology

161 

#### 3.1. Hydrological model

162 Top-SSF is a semi-distributed hydrological model based on the well-established

163 TOPMODEL framework, which delineates sub-basins based on the topographic index.

164 It retains the key advantages of TOPMODEL, such as its parsimonious structure,

批注 [L8]: RC1, Comment #4

165 physical interpretability, and ease of parameter transfer (Beven et al., 2021; Gao et al.,

批注 [L9]: RC1, Comment #5

166 2018), consists of 15 parameters representing six key hydrological components: canopy

167 interception, infiltration, evapotranspiration, unsaturated zone moisture transport,

168 subsurface storm flow, and flow routing (Li et al., 2024). In the Top-SSF model, flood

169 can be comprised of four components: infiltration-excess overland flow, saturation-

170 excess overland flow, subsurface storm flow, and groundwater discharge.

171 Infiltration-excess overland flow occurs when the rainfall intensity exceeds the  
172 infiltration capacity. In this study, infiltration is simulated using the Green-Ampt model.  
173 When surface ponding occurs, the infiltration rate is determined by solving the Green-  
174 Ampt equation iteratively, for which the Newton-Raphson method is employed. The  
175 infiltration rate ( $f_{in}$ ) is given by:

$$176 \quad f_{in} = -\frac{Ks(CD+F_{satrt})}{Szm(1-e^{(F_{satrt}/Szm)})} \quad (1)$$

177 where,  $f_{in}$  is the infiltration rate (m/h);  $Ks$  is surface hydraulic conductivity (m/h);  
178  $CD$  is capillary drive (m);  $F_{satrt}$  is the initial cumulative infiltration (m);  $Szm$  is the  
179 maximum water storage capacity in the unsaturated zone (m).

180 Saturation excess overland flow occurs at computational cell  $i$  when the  
181 groundwater table depth,  $S_i$  is less than or equal to zero (i.e.,  $S_i \leq 0$ , indicating the  
182 water table has reached the surface). It is calculated as:

$$183 \quad r_{s,i} = \max\{Suz_i - \max(S_i, 0), 0\} \quad (2)$$

184 where,  $r_{s,i}$  is the depth of saturation excess overland flow generated at cell  $i$  (m);  $Suz_i$   
185 is the soil water storage in the unsaturated zone, at cell  $i$  (m);  $S_i$  is the groundwater table  
186 depth at cell  $i$  (m).

187 The depth of subsurface storm flow generated at computational cell  $i$ ,  $r_{sf,i}$  is  
188 given by:

$$189 \quad r_{sf,i} = q_{sf0}(1 - S_{sf,i}/S_{fmax}) \quad (3)$$

190 where,  $r_{sf,i}$  is the depth of subsurface storm flow at cell  $i$  (m);  $q_{sf0}$  is initial subsurface  
191 storm flow (m);  $S_{sf,i}$  is the water storage deficit in the subsurface storm flow zone  
192 at cell  $i$  (m).

193 The depth of groundwater discharge is calculated as:

$$194 \quad r_b = e^{\ln Te - \lambda - \bar{S}_g/Szm} \quad (4)$$

195 where,  $r_b$  is depth of groundwater discharge (m);  $\ln Te$  is the log of the areal average of  
196  $T0$  ( $m^2/h$ ); is the catchment average topographic index;  $\bar{S}_g$  is the catchment average  
197 groundwater table depth (m). For the complete set of equations for the Top-SSF model,

198 the reader is referred to the Supplementary Material and (Li et al., 2024).

199

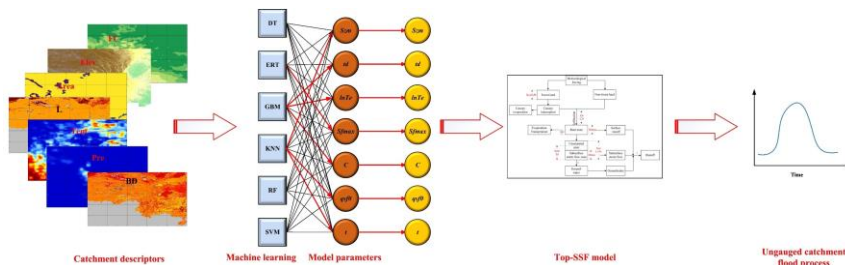
200 **3.2. Multi-machine learning ensemble method**

201 To improve flood prediction accuracy in ungauged mountainous catchments, we  
202 proposed a multi-machine learning ensemble method for regionalizing sensitive  
203 parameters of the Top-SSF model. This method leverages the complementary strengths  
204 of multi-machine learning methods to estimate model parameters based on catchment  
205 descriptors (Fig. 2). The characteristics, strengths, and limitations of each machine  
206 learning method are summarized in Table 2. The ensemble method employs a cross-  
207 validation procedure to select the best-performing machine learning method for each  
208 sensitive parameter. These selections are then integrated into a unified regionalization  
209 scheme. By mitigating limitations inherent in single machine learning regionalization,  
210 such as model bias and overfitting, and by capturing complex hydrological processes  
211 in mountainous catchment, this ensemble method aims to achieve more accurate flood  
212 prediction in ungauged catchments.

213

214 **Table 2.** Seven machine learning model characteristics, advantages and disadvantages.

Machine learning	Characteristic	Advantage	Disadvantages
DT	A single decision tree hierarchically partitions the data space using a tree structure, with internal nodes representing features, branches representing decision rules, and leaf nodes representing class labels.	High interpretability; Minimal data preprocessing.	Unstable; Tends to overfit.
ERT	Construct multiple decision trees with randomly selected feature values and randomly divided nodes (Geurts et al., 2006).	Low overfitting risk; Computational efficiency; Resilient to noise.	Possibility of increased bias; Limited interpretability.
GBM	Construct multiple decision trees. Multiple weak learners are trained iteratively and the loss function is optimised using gradient descent, progressively combined into a robust model through the learning rate (Friedman, 2002).	High accuracy for structured data; Robust to outliers; Minimal data preprocessing.	Limited interpretability; Complex adjustments.
KNN	It is a non-parametric, instance-based supervised learning algorithm. It operates by finding the K nearest data points in the training data to a given data point and making predictions based on these (Wani et al., 2017).	Simple and easy to implement. Learning process is quick.	Sensitivity to noisy and scale of data. Accuracy can be heavily impacted by the choice of K.
RF	A bagging algorithm proposed by Breiman (2001) that uses ensemble learning. Involves training numerous decision trees and aggregating predictions.	Simple and easy to implement; Low computational cost.	Prone to overfitting in noisy regression tasks.
SVM	Identifies hyperplanes in high-dimensional spaces to segregate data. The optimal hyperplane maximizes the margin between it and the nearest data points, termed support vectors (Sain, 1996).	Uses kernel functions to address nonlinear classification issues.	Sensitive to noise



215

216 **Fig.2.** Multi-machine learning ensemble method for regionalization in ungauged mountainous  
217 catchments. The red line indicates the machine learning method that yielded the optimal  
218 parameter estimates.

批注 [L10]: RC2, Comment#8

### 219 **3.3. Parameter regionalization process**

220 The parameter regionalization process comprised four key steps: (1) Top-SSF  
221 model calibration and parameter sensitivity analysis; (2) selection of relevant catchment  
222 descriptors; (3) establishment of regionalization relationships between sensitive model  
223 parameters and catchment descriptors using multi-machine learning ensemble methods;

224 and (4) evaluation of parameter regionalization performance.

225 **3.3.1. Top-SSF model calibration and parameter sensitivity analysis**

226 In this study, the Top-SSF model was employed to simulate hydrological processes.

227 The model was driven by continuous hourly meteorological data, including rainfall,

228 temperature, surface pressure, relative humidity, wind speed, and surface net solar

229 radiation. For each catchment, model parameters were calibrated using two

230 hydrologically independent and representative flood events. A third, distinct flood

231 event was then used for model validation. The Nash-Sutcliffe Efficiency (NSE) served

批注 [L11]: RC1, Comment#5

232 as the objective function during calibration, with parameter optimization achieved

233 using the Shuffled Complex Evolution (SCE-UA) algorithm (Duan et al., 1994), known

234 for its global convergence and robustness (Dakhlaoui et al., 2012; Qi et al., 2016).

235 Model performance was evaluated using the NSE, the relative error of flood peak flow

236 (Q<sub>p</sub>), and the absolute error in flood peak occurrence time (T<sub>p</sub>), following China's

批注 [L12]: RC2, Comment#9

237 Specification for Hydrological Information Forecast (GB/T 22482-2008). These

238 metrics quantify the model's ability to predict flood dynamics, peak flow, and timing.

239 Following calibration, a sensitivity analysis was conducted to identify and exclude

240 insensitive model parameters (Lenhart et al., 2002), which were then used for

241 regionalization. This approach reduces the dimensionality of the regionalization

242 problem and improves the efficiency of the process.

243 The sensitivity index (*Si*) of each hydrological model parameter was determined

244 using the method of Lenhart et al. (2002), which assesses the influence of  $\pm 10\%$

245 changes in parameter values (Eq. 1). Table 3 outlines the sensitivity analysis results for

246 the model parameters across the 80 mountainous catchments. The  $Si$  values are  
 247 categorized as follows (Guo et al., 2022): negligible sensitivity ( $|Si| < 0.05$ ),  
 248 moderate sensitivity ( $0.05 < |Si| < 0.2$ ), high sensitivity ( $0.2 < |Si| < 1.00$ ), and  
 249 extremely high sensitivity ( $|Si| \geq 1.00$ ). Based on the sensitivity analyses, seven  
 250 sensitive model parameters were identified:  $Szm$ ,  $lnTe$ ,  $Sfmax$ ,  $C$ ,  $qsf0$ ,  $t$  (Table 3).

251 
$$Si = \frac{1}{N} \sum_t^N \frac{(y_2(t) - y_1(t))/y_0(t)}{2\Delta x/x_0} \quad (5)$$

252 where  $y_0(t)$  is the flood value of the calibrated parameter  $x_0$  at time  $t$ ;  $\Delta x$  is the  
 253 adjusted parameter difference,  $\Delta x/x_0=10\%$ ;  $y_1(t)$  is the flood value of the calibrated  
 254 parameter  $x_0 - \Delta x$  at time  $t$ ;  $y_2(t)$  is the flood value of the calibrated parameter  $x_0 +$   
 255  $\Delta x$  at time  $t$ .

256 **Table 3.** Top-SSF model main modules and default range of parameters.

Modular	Parameter	Definition	Unit	Default range	Sensitivity index
Canopy interception	$Sc$	Canopy storage capacity	m	0.00~0.01	<0.05
	$St$	Trunk storage capacity	m	0.00~0.01	<0.05
	$Pt$	Proportion of rain diverted into stemflow per cover	%	0.00~1.00	<0.05
Evapotranspiration	$Sr0$	Initial root zone storage deficit	m	0.00~0.02	<0.05
	$Srmax$	Maximum root zone storage deficit	m	0.00~2	<0.05
Infiltration	$Ks$	Surface hydraulic conductivity	m/h	0~0.01	<0.05
	$CD$	Capillary drive (Morel-Seytoux et al., 1974)	m	0~5	<0.05
Unsaturated zone	$Suz0$	Initial baseflow per unit area	m	0.00~ $10^{-4}$	<0.05
	$Szm$	Soil maximum water storage capacity	m	0.00~1.00	<b>0.19</b>
	$td$	Unsaturated zone time delay per unit storage deficit	h/m	0~3	<b>1.07</b>
	$lnTe$	log of the areal average of $T0$	$m^2/h$	-2.00~1.00	<b>3.4</b>
Subsurface storm flow zone	$Sfmax$	Maximum subsurface storm flow zone deficit	m	0.00~0.01	<b>0.16</b>
	$C$	Transfer coefficient	$m^2/h$	0.00~0.1	<b>0.26</b>
	$qsf0$	Initial subsurface storm flow per unit area	m	0.00~0.02	<b>0.18</b>
Routing	$t$	Flow routing correction coefficient	-	0.00~5.0	<b>1.21</b>

257 Note, the bolded values in the sensitivity index indicate sensitive model parameters.

258 **3.3.2. Catchment descriptor selection**

259 To mitigate the effects of multicollinearity on the accuracy and reliability of the  
260 parameter regionalization methods, catchment descriptors were screened using the  
261 variance inflation factor (VIF) and correlation coefficients. A VIF threshold of less than  
262 10 ( $VIF < 10$ ) was used to indicate acceptably low multicollinearity (Salmeron et al.,  
263 2018). Initial screening identified strong correlations between several descriptor pairs,  
264 notably L with  $Ks\_CH$ , and  $Tem$  with  $Elev$ . Furthermore, the VIF values for  $Ks\_CH$   
265 and  $Slope$  were found to exceed 10. Consequently,  $Ks\_CH$  and  $Slope$  were removed  
266 from the potential set of descriptors. Following their removal, a re-evaluation of the  
267 VIF for the remaining descriptors was conducted. Although a notable correlation exists  
268 between  $Tem$  and elevation ( $Elev$ ), their VIF values in the reduced set were both below  
269 the threshold of 10. Given the importance of  $Tem$  for representing climate impacts and  
270  $Elev$  as a key topographic driver, both were retained to preserve potentially valuable  
271 information. The final set of seven catchment descriptors selected for regionalization  
272 therefore comprised  $FC$ ,  $Elev$ ,  $Area$ ,  $L$ ,  $Tem$ ,  $Pre$ , and  $BD$ . As illustrated in Fig. 3b, the  
273 correlations among these final descriptors and the sensitive model parameters are  
274 generally low (highest at 0.5), suggesting that the relationships are complex and  
275 nonlinear.



276  
277 **Fig.3.** Analysis of catchment descriptor relationships: (a) Correlation coefficients and variance  
278 inflation factors (VIF) among all descriptors; (b) Correlation coefficients between  
279 sensitivity model parameters and descriptors with VIF values below 10.

### 280 3.3.3. Parameter regionalization

281 To simulate ungauged catchment conditions, each of the 80 catchments was  
282 iteratively treated as an ungauged catchment, with the remaining 79 catchments serving  
283 as donor catchments. A parameter regionalization method was then constructed using  
284 the catchment descriptors and sensitive model parameters of the donor catchments to  
285 predict the seven sensitive model parameters for the ungauged catchment based on its  
286 catchment descriptors. These predicted model parameters were then input into the Top-  
287 SSF model to enable flood prediction in ungauged catchments. To ensure robust and  
288 generalizable results, K-fold cross-validation ( $K = 10$ ) was implemented. This involved  
289 randomly partitioning the 79 donor catchments into  $K$  subsets, using one subset as a  
290 test set and the remaining  $K-1$  subsets for method training in each iteration (Jung, 2018).  
291 This approach maximizes data utilization and minimizes bias associated with specific  
292 data partitioning. Hyperparameter tuning for each machine learning method was  
293 performed using RandomizedSearchCV (Bergstra et al., 2012), with the objective of  
294 minimizing the difference between predicted and observed parameter values.

295 **3.3.4. Evaluated metrics**

296 The performance of the parameter regionalization methods was evaluated by  
 297 considering two key aspects. First, the accuracy of the methods in estimating sensitive  
 298 model parameters was assessed using three metrics: root mean square error (RMSE),  
 299 standard deviation (STD), and the coefficient of determination ( $R^2$ ). The  $R^2$  was used  
 300 to quantify the agreement between estimated and calibrated parameter sets. Second, to  
 301 evaluate the impact of parameter regionalization on flood prediction. The resulting  
 302 flood predictions were then evaluated using the NSE,  $Q_p$ , and  $T_p$  metrics.

$$303 NSE = 1 - \frac{\sum_{j=1}^M (Q_{obs}(j) - Q_{sim}(j))^2}{\sum_{j=1}^M (Q_{obs}(j) - \bar{Q}_{obs})^2} \quad (6)$$

$$304 Q_p = \left| \frac{Q_{obs,p} - Q_{sim,p}}{Q_{obs,p}} \times 100\% \right| \quad (7)$$

$$305 T_p = |T_{obs,p} - T_{sim,p}| \quad (8)$$

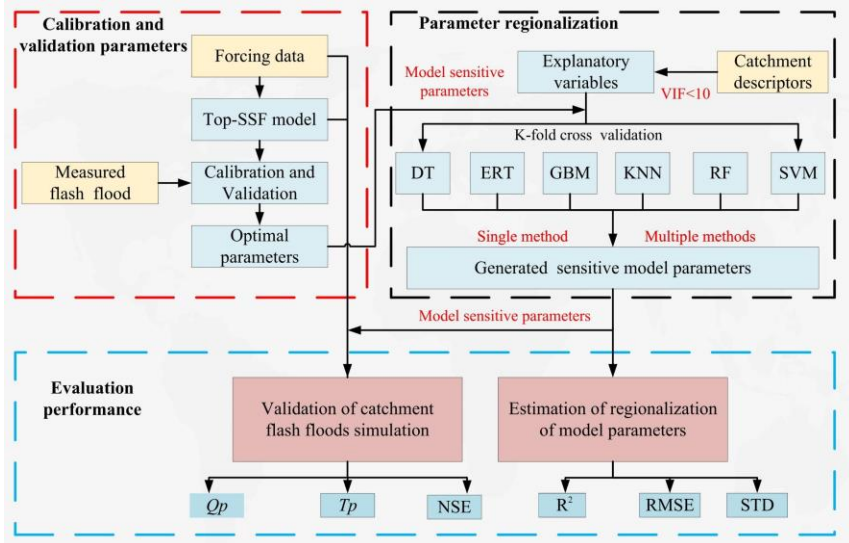
306 where  $Q_{obs}(j)$  is the observed flow rate ( $m^3/s$ );  $Q_{sim}(j)$  is the simulated flow rate  
 307 ( $m^3/s$ );  $\bar{Q}_{obs}$  is the mean value of the observed flow rate ( $m^3/s$ );  $Q_{obs,p}$  is the observed  
 308 flood peak flow ( $m^3/s$ );  $Q_{sim,p}$  is the simulated flood peak flow ( $m^3/s$ );  $T_{obs,p}$  is the  
 309 observed flood peak occurrence time (h); and  $T_{sim,p}$  is the simulated flood peak  
 310 occurrence time (h).

$$311 \quad 312 RMSE = \sqrt{\frac{1}{N} \sum_{i=1}^n (X_i - Y_i)^2} \quad (9)$$

$$313 STD = \sqrt{\frac{1}{N-1} \sum_{i=1}^N (Y_i - \bar{Y})^2} \quad (10)$$

$$314 R^2 = \frac{[\sum_{i=1}^n (X_i - \bar{X})(Y_i - \bar{Y})]^2}{\sum_{i=1}^n (X_i - \bar{X})^2 \sum_{i=1}^n (Y_i - \bar{Y})^2} \quad (11)$$

315 where  $X_i$  is the Top-SSF calibration model parameter value;  $Y_i$  is the model parameter  
 316 estimated value using the parameter regionalization method;  $\bar{X}$  and  $\bar{Y}$  are the mean  
 317 values of  $X_i$  and  $Y_i$ ;  $N$  is the sample size equal to 80.



318

319 **Fig.4.** Flowchart illustrating the parameter calibration, validation, and regionalization workflow.

320 Abbreviations: Top-SSF (Topography-Based Subsurface Storm Flow hydrological model),  
 321 DT (Decision Tree), ERT (Extremely Randomized Trees), GBM (Gradient Boosting  
 322 Machine), KNN (K-Nearest Neighbor), RF (Random Forest), SVM (Support Vector  
 323 Machine), NSE (Nash-Sutcliffe efficiency),  $R^2$  (Coefficient of Determination), Qp (The  
 324 relative error of flood peak flow), Tp (The absolute error in flood peak occurrence time),  
 325 VIF (Variance inflation factor), RMSE (Root mean square error), STD (Standard  
 326 deviation).

327 

## 4. Result

328 

### 4.1. Model performance

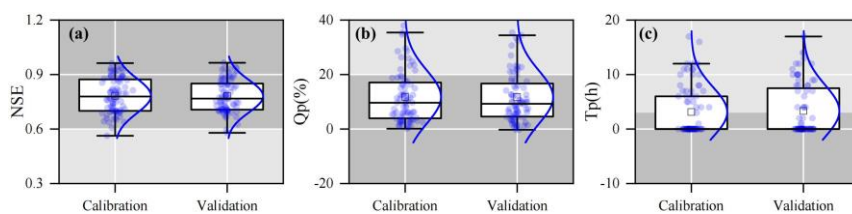
329 The Top-SSF model demonstrated good flood simulation performance across the  
 330 80 gauged catchments, as quantified by NSE, Qp, and Tp. During the calibration period,  
 331 50% of the catchments achieved NSE values exceeding 0.78 (Fig. 5a), the median Qp  
 332 value was below 10% (Fig. 5b), and the median Tp value was within 2 hours (Fig. 5c).  
 333 The average NSE value was approximately 0.8, with a maximum of 0.96. The majority  
 334 of Qp values were around 8%, and the majority of Tp values were below 2 hours.  
 335 During the validation period, the median NSE value was 0.76 (Fig. 5a), the median Qp

336 value was below 10% (Fig. 5b), and the median Tp value was within 4 hours (Fig. 5c).

337 The hydrological response times for the 80 catchments were approximated as the time  
338 from precipitation peak to flood peak. The estimated range is from 1 to 26 hours. This  
339 diversity is indicative of the comprehensive nature of the study, which encompasses  
340 both rapid flash floods in smaller basins and more general floods in larger, mountainous  
341 catchments (mean area: 1,586 km<sup>2</sup>). For catchments with longer response times, a  
342 median error of 2-4 hours remains operationally valuable for providing sufficient flood  
343 warning lead time. It is noteworthy that the median Tp during the calibration period  
344 (within 2 hours) satisfied China's Specification for Hydrological Information Forecast  
345 (GB/T 22482-2008) stringent requirements for high-quality forecasts.

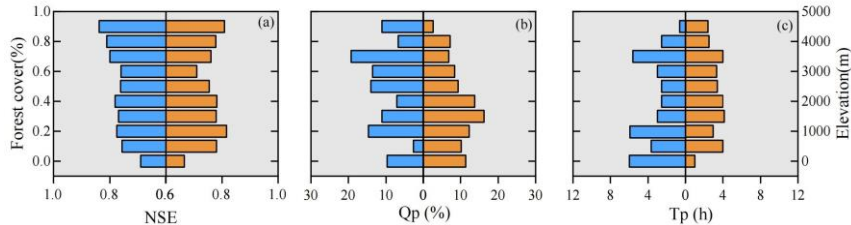
批注 [L13]: RC2, Comment#10

346 Model performance also exhibited some dependence on catchment characteristics.  
347 For instance, NSE generally improved with increasing forest cover (Fig. 6a), potentially  
348 due to the model's explicit representation of forest canopy interception and subsurface  
349 storm flow generation mechanisms. The relationship between NSE, Qp, Tp and  
350 elevation was more complex, suggesting a nonlinear influence of elevation on model  
351 performance (Fig. 6 a-c). The demonstrated robust performance of the Top-SSF model  
352 provides a strong foundation for its application in subsequent parameter regionalization  
353 analyses.



354  
355 **Fig. 5.** Boxplots of (a) NSE, (b) Qp, and (c) Tp during the calibration and validation periods

356 for 80 gauged catchments. The box represents the interquartile range, with the middle line  
 357 indicating the median (50th percentile). The whiskers represent the minimum and  
 358 maximum values. "□" represents the mean value. Dark grey indicates the range of flood  
 359 prediction criteria (i.e.,  $NSE > 0.75$ ,  $Qp < 20\%$ , and  $Tp < 2$  hours).



360  
 361 **Fig.6.** Influence of environmental factors on Top-SSF model performance in flood simulation. The  
 362 graphs illustrate the relationship between model evaluation metrics and forest cover (left) and  
 363 elevation (right)."

#### 364 **4.2. Results of parameter regionalization**

##### 365 **4.2.1. Comparison of sensitive model parameter estimates**

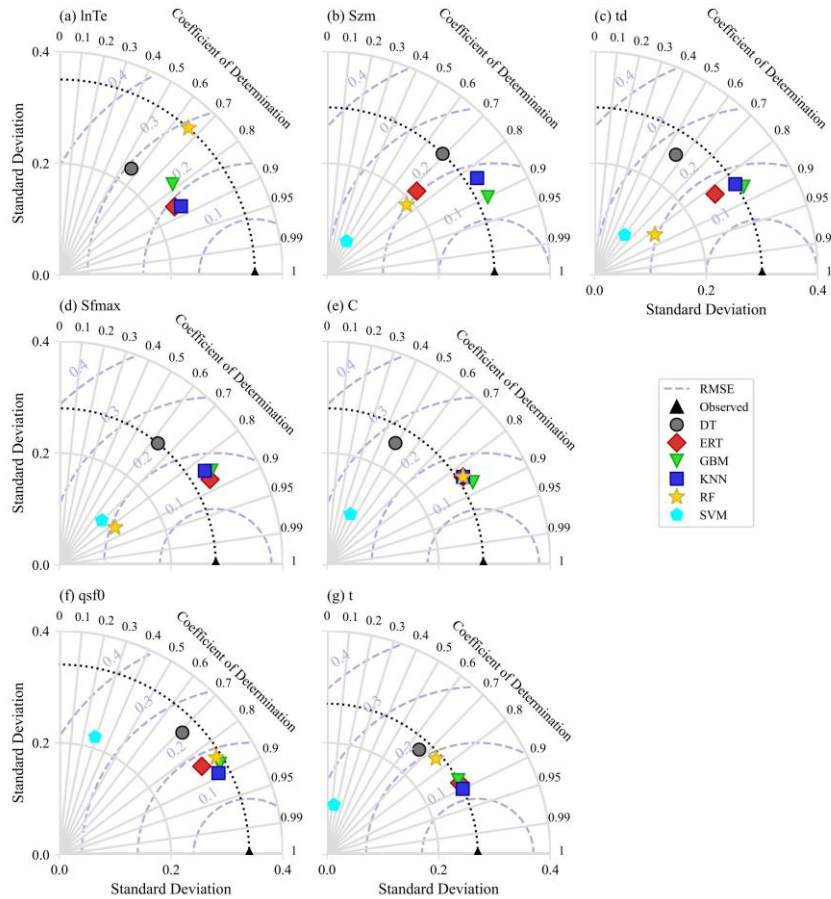
366 The six single machine learning regionalization methods exhibited varying  
 367 performance in estimating sensitive model parameters (Fig. 7), likely due to differences  
 368 in catchment descriptor characteristics and the underlying principles of each method.

370 Their hyperparameter results are presented in Tables S1–S6 of the supplementary

371 material. The GBM demonstrated the highest accuracy in estimating  $Szm$ ,  $td$ , and  $C$   
 372 ( $R^2 = 0.90$ ,  $0.86$ , and  $0.87$ , respectively,), with its estimates also exhibiting a STD that  
 373 closely matched the distribution of the calibrated parameter values. KNN provided the  
 374 most accurate estimates for  $lnTe$ ,  $qsf0$ , and  $t$  ( $R^2 = 0.87$ ,  $0.89$ , and  $0.90$ , respectively),  
 375 also with STD closely resembling the calibrated parameter distributions. ERT  
 376 performed best in estimating  $Sfmax$  ( $R^2 = 0.87$ ), but its performance was generally  
 377 poorer for other parameters. DT, SVM, and RF methods generally showed lower  
 378 performance across all sensitive model parameters. These differences in performance  
 379 highlight the potential benefits of multi-machine learning ensemble methods for

批注 [L14]: RC 2, Comment # 14

380 improving flood prediction in ungauged mountainous catchments.



381

382 **Fig.7.** Performance of parameter regionalization methods assessed using Taylor diagrams. The  
383 diagrams show the accuracy of sensitive model parameter estimates, with the coefficient  
384 of determination ( $R^2$ ) indicated by the radial axis, standard deviation (STD) by the  
385 horizontal and vertical axes, root mean square error (RMSE) by the grey-blue dotted lines,  
386 and the standard deviation of observations by the black dotted line."

#### 387 4.2.2. Comparison of flood forecasting results

388 The flood prediction performance of the Top-SSF model, integrated with different  
389 parameter regionalization methods, was compared across 80 mountainous catchments  
390 in southwestern China. The methods included single machine learning methods and a

391 multi-machine learning ensemble method (GBM-KNN-ERT), where GBM estimated  
392  $S_{zm}$ ,  $td$ , and  $C$ ; KNN estimated  $\ln Te$ ,  $qsf0$ , and  $t$ ; and ERT estimated  $Sfmax$ . The  
393 performance of these parameter regionalization methods was then evaluated against the  
394 performance of the Top-SSF model using calibrated parameters. Among the single  
395 machine learning methods, GBM performed best, with 60 catchments achieving a  
396 positive NSE (NSE > 0, Fig. 8d). Critically, for high-accuracy predictions (NSE > 0.9),  
397 GBM succeeded in 43 catchments (54%), also showing strong performance with  $Q_p$   
398 less than 5% and  $T_p$  less than 1 hour in most cases (Fig. 8a-c). The GBM-KNN-ERT  
399 ensemble method yielded even better results. It increased the number of catchments  
400 with positive NSE to 75 (Fig. 8d). More impressively, the ensemble method achieved  
401 exceptional performance (NSE > 0.9) in 72 catchments (90%). This represents a 67.44%  
402 increase in the number of high-accuracy predictions compared to the best single method  
403 (GBM). Furthermore, the ensemble method  $Q_p$  values were more concentrated around  
404 zero, and 90% of catchments maintained near-zero  $T_p$  values. These results strongly  
405 demonstrate the superior potential of multi-machine learning ensembles for improving  
406 flood prediction in ungauged catchments.

批注 [L15]: RC1, Comment 6

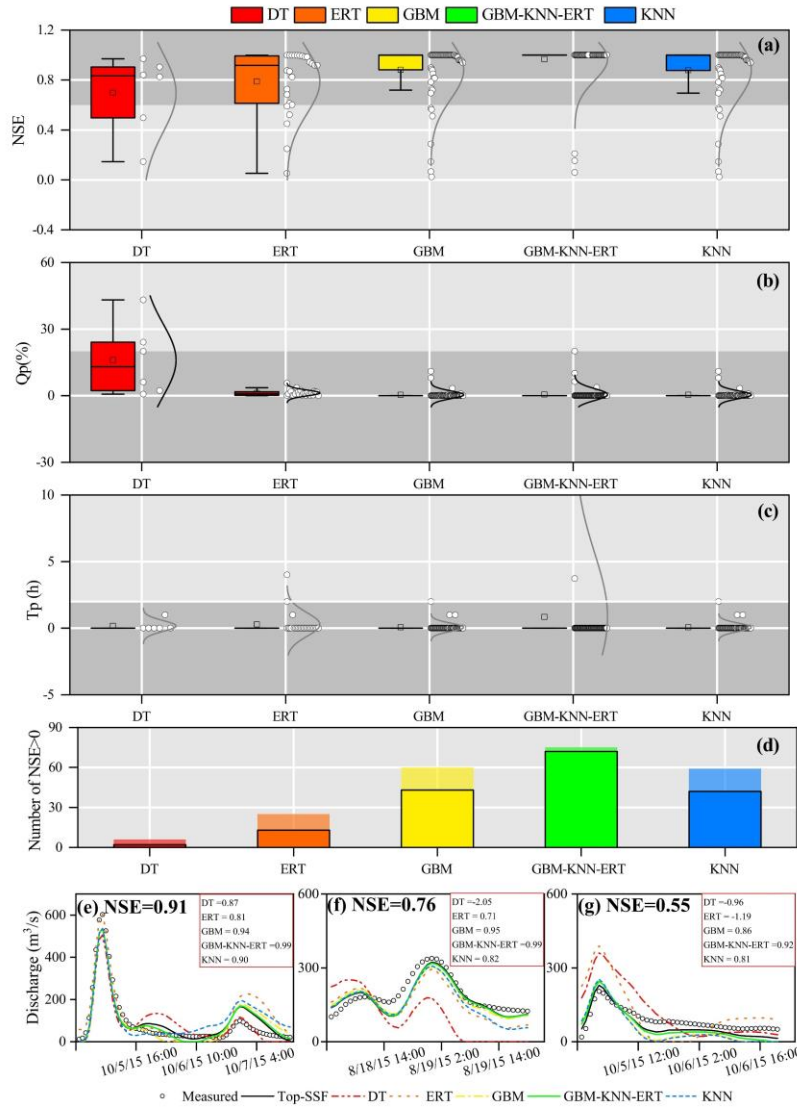
407 To further illustrate these performance differences visually, Fig. 8 (e, f, and g)  
408 presents hydrographs from three randomly selected flood events. These events  
409 represent cases where the calibrated Top-SSF model itself achieved high (NSE=0.91),  
410 medium (NSE=0.76), and low (NSE=0.55) performance, respectively. A key insight  
411 from these plots is that the Top-SSF simulation (solid black line) is the performance  
412 benchmark for the regionalization methods. Although the models aim to approximate

批注 [L16]: RC2, Comment#14

413 measured floods, their performance is ultimately limited by the accuracy of the Top-  
414 SSF model structure and its optimized parameters.

415 The hydrographs show how the GBM-KNN-ERT ensemble achieves superior  
416 performance by leveraging the complementary strengths of its component methods. For  
417 instance, in the high-performance case (Fig. 8e), the GBM and KNN methods capture  
418 the overall shape well, but the ERT simulation provides a more precise estimation of  
419 the primary flood peak. The final ensemble successfully integrates this peak accuracy,  
420 resulting in the highest overall performance. Similarly, Fig. 8f shows that the ensemble  
421 moderates the slow initial rise characteristic of the KNN method, leading to a more  
422 realistic rising limb. The ensemble method ability to balance competing errors is most  
423 evident in the low-performance case (Fig. 8g). During the recession phase, the ensemble  
424 method averages the high bias of the ERT method with the low bias of the GBM and  
425 KNN methods, producing a hydrograph that more closely resembles the benchmark  
426 simulation than any single model could. This synergy demonstrates that the ensemble  
427 method superior performance is a direct result of its ability to integrate the specific,  
428 complementary strengths of each member model across different parts of the  
429 hydrological process.

批注 [L17]: RC2, Comment#16



430  
431 **Fig.8.** Evaluation of flood prediction performance for different parameter regionalization  
432 methods. (a-c) show the distributions of Nash-Sutcliffe Efficiency (NSE), relative peak  
433 flow error (Qp), and peak time error (Tp) across all 80 catchments, with shaded regions  
434 indicating where flood prediction standards were met (NSE > 0.75, Qp < 20%, and Tp <  
435 2 hours). (d) shows the number of catchments with NSE > 0 and the black border indicates  
436 the number of catchments with NSE > 0.9. (e-g) present example hydrographs comparing  
437 the simulated flood from each regionalization method against measured flood flow and  
438 the calibrated Top-SSF model benchmark for catchments where the benchmark model  
439 performance was (e) high (NSE=0.91), (f) medium (NSE=0.76), and (g) low (NSE=0.55).

440 **5. Discussion**

441 **5.1. Reliability of multi-machine learning ensemble in parameter regionalization**

442 In this study, the GBM-KNN-ERT method demonstrated superior regionalization  
443 performance, highlighting the potential of ensemble methods for improving  
444 hydrological predictions in ungauged mountainous catchments. The success of the  
445 ensemble is rooted in the distinct learning mechanisms and behaviors of its individual  
446 components, which were revealed during hyperparameter optimization.

447 The GBM method exhibited distinct parameter-specific sensitivities to  
448 hyperparameters (Fig. 9a-c). For parameter  $C$ , the negative correlation between  $R^2$  and  
449  $n_{\text{estimators}}$  ( $>300$  trees) indicates overfitting risks when modeling complex rainfall-  
450 runoff interactions in heterogeneous mountainous terrain (Fig. 9a). This aligns with  
451 previous findings emphasizing the need for complexity control in hydrological  
452 generalization (Schoups et al., 2008). Conversely, the improved  $R^2$  for parameter  $td$   
453 with increased  $n_{\text{estimators}}$  highlights the capacity of ensemble learning to capture  
454 complex, nonlinear relationships between catchment descriptors and hydrological  
455 parameters (Hastie et al., 2009). The contrasting optimal  $\text{max\_depth}$  of 5 layers for  
456 parameter  $C$ , compared to shallower optimal depths (3 layers) for  $Szm$  and  $td$ , suggests  
457 that parameters governing more complex hydrological processes in mountainous  
458 catchments may require deeper decision trees to effectively capture the interactions  
459 between climate, topography, and soil properties (Wainwright et al., 2013).

460 KNN performance exhibited pronounced sensitivity to neighbourhood size  
461 ( $n_{\text{neighbors}}$ ) and distance metric ( $p$ ), highlighting the spatial heterogeneity of

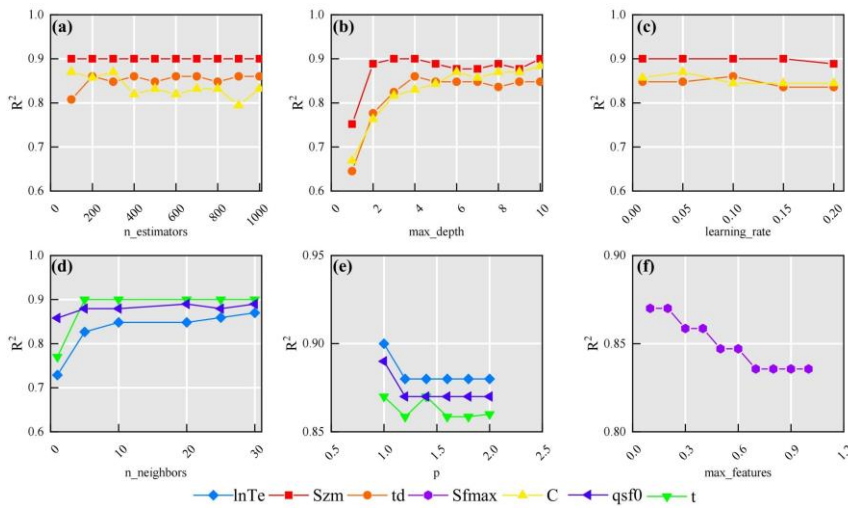
462 catchment descriptors. For parameters *lnTe* and *qsf0*, optimal performance was  
463 observed at *n\_neighbors* =30 (Fig. 9d), aligns with the hypothesis that meaningful  
464 hydrological similarities can emerge even in topographically complex mountainous  
465 regions when considered at broader spatial scales (Li et al., 2022). Conversely,  
466 parameter *t* achieved peak accuracy at *n\_neighbors*=5, suggesting that localized, short-  
467 term weather events and fine-scale topographic similarities in adjacent mountainous  
468 areas can significantly influence local runoff processes (Garambois et al., 2015). The  
469 Manhattan distance metric (*p*=1) outperformed Euclidean distance across all  
470 parameters (Fig. 9e). This superiority stems from its ability to mitigate the "curse of  
471 dimensionality" (Bellman, 1961) in high-dimensional datasets, a common  
472 characteristic of mountainous catchments. In such datasets, sparse data distributions  
473 and the presence of mixed variable types (e.g., topographic indices, land cover) can  
474 significantly degrade the discriminative power of Euclidean distance (Rockström et al.,  
475 2023). The robustness of the Manhattan distance arises from its axis-aligned sensitivity,  
476 which provides a more effective means of handling feature scaling and integrating  
477 catchment descriptors compared to the radial symmetry of Euclidean distance.

478 ERT performance was maximized at *max\_features* = 0.15 (Fig. 9f). By restricting  
479 the random sampling of features during node splits (using only 15% of the features),  
480 both the diversity of the trees was enhanced and the effects of multicollinearity between  
481 topographic and soil attributes were reduced. This finding aligns with the theory  
482 proposed by Geurts et al. (2006), which suggests that random feature selection can  
483 significantly improve model generalization, a particularly important consideration in

484 ungauged mountainous catchments characterized by high levels of inter-correlation  
 485 among predictor variables.

486 These distinct sensitivities and learning mechanisms form the scientific basis for  
 487 the superiority of the GBM-KNN-ERT method. As shown in Section 4.2, no single  
 488 machine learning method is universally optimal for all hydrological model parameters.  
 489 Instead, the ensemble method effectively allocates each parameter to the model best  
 490 suited for its regionalization. Specifically, GBM, with its capacity for modeling  
 491 complex interactions, proved optimal for integrated parameters like *Szm* and *td*. In  
 492 contrast, the instance-based KNN was superior for parameters like *lnTe*, which are  
 493 governed by physical similarity and spatial coherence. Finally, the highly randomized  
 494 nature of ERT provided the necessary robustness to model the noisy relationship  
 495 associated with the *Sfmax*. This synergistic combination, where each model  
 496 contributes its unique strength, results in a final regionalization framework that is more  
 497 accurate and physically plausible than any individual method operating in isolation.

批注 [L18]: RC2, Comment# 13



498

499 **Fig.9.** Sensitivity of parameter estimation performance to key hyperparameters in (a-c) GBM,  
500 (d-e) KNN method, and (f) ERT. (a) *n\_estimators* (number of decision trees in GBM), (b)  
501 *max\_depth* (maximum depth of decision trees in GBM), (c) learning rate (GBM), (d)  
502 *n\_neighbors* (number of neighbors in KNN), (e) *p*-value of Minkowski distance (KNN;  
503 *p*=1: Manhattan distance, *p*=2: Euclidean distance), and (f) *max\_features* (ERT).

504 **5.2. Combining multiple machine learning methods for parameter regionalization**

505 Machine learning methods exhibit distinct strengths in hydrological parameter  
506 estimation due to fundamental differences in data processing mechanisms, pattern  
507 recognition strategies, and prediction generation (Bishop et al., 2006). This suggests  
508 that multi-machine learning ensemble methods have the potential to synergistically  
509 integrate advantages while effectively compensating for individual limitations, leading  
510 to more robust and accurate parameter estimates. As demonstrated in Fig. 10, the GBM-  
511 KNN-ERT method achieved notable improvements over any single machine learning  
512 method, particularly for sensitive parameters *lnTe*, *Sfmax*, *qsf0* and *t*, with  $R^2$   
513 increases ranging from 0.02 to 0.03 compared to the best-performing GBM method  
514 (Fig.10e).

515 Interestingly, a comparison of GBM4-KNN3 (where *Sfmax* is estimated by GBM)  
516 and GBM3-KNN4 (where *Sfmax* is estimated by KNN) revealed critical insights into  
517 model parameter compatibility. Despite both achieving an identical  $R^2$  of 0.85 for the  
518 estimation of *Sfmax*, GBM4-KNN3 exhibited superior flood prediction performance,  
519 with 72 catchments achieving  $NSE > 0$  compared to only 68 catchments for GBM3-  
520 KNN4. This suggests that GBM possesses an enhanced capability to resolve the  
521 complex coupling between soil moisture dynamics and topography, leading to more  
522 physically plausible representation of subsurface storm flow processes (Gupta et al.,  
523 2023). The wider distribution of flood prediction performance observed for GBM3-

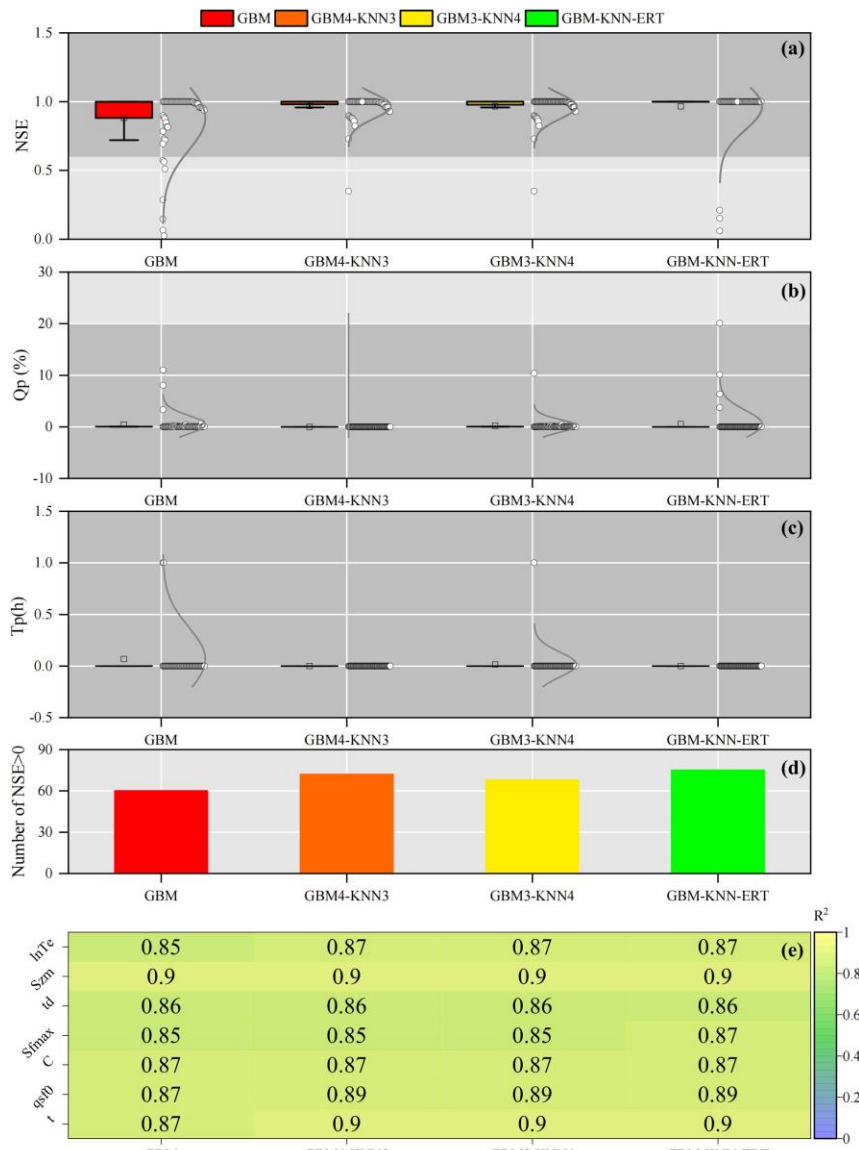
524 KNN4 (Fig. 10 a–c) further suggests that uncertainties introduced by KNN in the  
525 estimation of  $Sfmax$  may propagate nonlinearly during flood simulations, potentially  
526 amplifying errors. This observation aligns with theoretical expectations that distance-  
527 based methods may tend to oversmooth critical thresholds or sharp transitions in  
528 heterogeneous environments, leading to a less accurate representation of hydrological  
529 responses (Bellman, 1961).

530 Furthermore, an important consideration in adopting ensemble methods is the  
531 trade-off between predictive accuracy and computational efficiency. To evaluate this  
532 trade-off, we compared the model training times for various parameter regionalization  
533 methods, with the results summarized in Table 4. The analysis shows that our proposed  
534 GBM-KNN-ERT ensemble, while providing the highest predictive accuracy, required  
535 a total training time of 102.8 s. This is moderately higher than the best-performing  
536 single model, GBM (57.6 s), and other simpler ensemble methods like GBM4-KNN3  
537 (36.1 s). The increased computational time for the GBM-KNN-ERT method is  
538 primarily attributed to the inclusion of the ERT method for estimating the  $Sfmax$ ,  
539 which is inherently more computationally intensive than GBM or KNN.

540 However, it is crucial to contextualize this computational cost for operational use.  
541 The process of training a regionalization method is an offline task, performed once to  
542 establish the stable relationships between catchment descriptors and model parameters.  
543 This one-time investment is not a constraint on real-time flood forecasting, as once the  
544 method is trained, parameter estimation for a new ungauged catchment is nearly  
545 instantaneous. Given this context, the modest increase in one-time training cost is a

546 justifiable investment for the significant improvements achieved in flood prediction  
547 accuracy, model robustness, and stability. Therefore, for applications in water resource  
548 management and flood risk assessment where high accuracy is paramount, the GBM-  
549 KNN-ERT method strikes an optimal and practical balance between computational  
550 efficiency and predictive performance.

批注 |L19|: RC2 Comment#3



551  
552 **Fig.10.** Assessment of combined machine learning methods for improved parameter  
553 regionalization in ungauged mountainous catchments. Performance is evaluated against  
554 the GBM method, showing (a) NSE, (b) Qp, (c) Tp, (d) Number of catchments with NSE >  
555 0, and (e) the difference in  $R^2$ .

556  
557  
558  
559

560 **Table 4.** Running time (s) for different parameter regionalization methods

批注 [L20]: RC1 Comment#3

	GBM	GBM4-KNN3	GBM3-KNN4	GBM-KNN-ERT	KNN	ERT
<i>lnTe</i>	11.3	3.4	3.4	3.7	3.6	74.4
<i>Szm</i>	7.8	7.5	7.7	7.8	0.6	76.7
<i>td</i>	8.2	8.1	8.0	8.5	0.6	74.7
<i>Sfmax</i>	7.7	8.2	0.6	73.6	0.5	74.9
<i>C</i>	7.8	7.7	7.7	8.0	0.6	74.9
<i>qsf0</i>	7.4	0.6	0.6	0.6	0.6	76.3
<i>t</i>	7.4	0.6	0.6	0.6	0.5	75.3
Sum	57.6	36.1	28.6	102.8	7.0	527.2

561

562 **5.3. The influence of donor catchment quantity on machine-learning parameter**  
563 **regionalization**

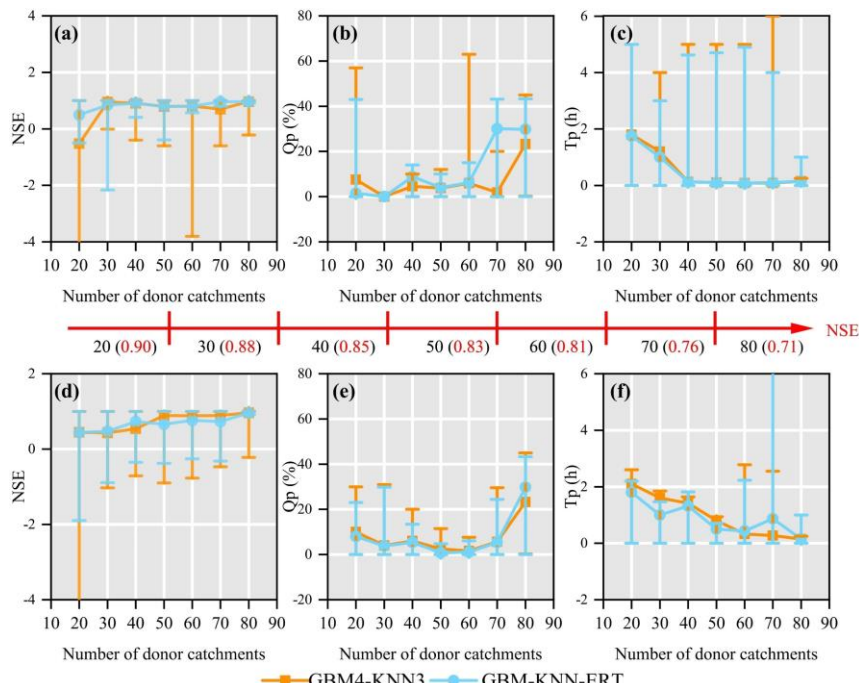
564 The number of donor catchments used in machine learning-based parameter  
565 regionalization methods is a critical factor influencing the accuracy and robustness of  
566 hydrological predictions in ungauged catchments (Gauch et al., 2021; Song et al., 2022;  
567 Zhang et al., 2022). In this study, we investigated the influence of donor catchment  
568 quantity (ranging from 20 to 80) on the flood prediction performance of the two best-  
569 performing parameter regionalization methods (GBM4-KNN3 and GBM-KNN-ERT)  
570 across the 80 mountainous catchments (Fig 11). It is important to clarify that the  
571 following analysis is not a method for selecting donor catchments based on physical  
572 similarity—a task handled by the machine learning methods itself when it learns the  
573 relationships between catchment descriptors and model parameters. Instead, this  
574 experiment serves as a sensitivity analysis to understand how the regionalization  
575 performance is affected by the overall quantity and quality of the available training data.

批注 [L21]: RC2, Comment#12

576 To systematically investigate the performance influence of donor catchment  
577 quantity on parameter regionalization, two distinct sampling strategies were employed  
578 across the 80 mountainous catchments. In Mode 1 (selection of donor catchments based  
579 on decreasing NSE), which was designed to test the impact of data quality, a non-

580 monotonic relationship was observed. For both methods, regionalization performance  
581 peaked with 20-40 donor catchments and then declined, particularly for the GBM4-  
582 KNN3 method (Fig. 11a-c). This performance degradation is not due to increasing  
583 catchment dissimilarity, but rather to the introduction of lower-quality training data. As  
584 the donor pool expands beyond the best-performing catchments, it begins to include  
585 catchments where the Top-SSF model calibration itself was less successful (i.e., lower  
586 NSE values). These 'low-quality' samples may introduce noise and less reliable  
587 parameter-descriptor relationships, which can mislead the training process (Gauch et  
588 al., 2021; Zhang et al., 2022). Notably, the GBM-KNN-ERT method demonstrated  
589 greater resilience to this degradation. Its performance, while also peaking early, did not  
590 degrade as sharply and instead tended to stabilize after the inclusion of approximately  
591 70 catchments. This suggests that the more complex ensemble structure has a superior  
592 ability to suppress noise and generalize from a dataset containing a mix of high- and  
593 low-quality examples, highlighting its enhanced robustness. In contrast, Mode 2  
594 (random selection of donor catchments) demonstrated a consistent improvement in  
595 regionalization performance for both NSE and Tp as the number of donor catchments  
596 increased (Fig. 11d-f). However, while the average performance improves with data  
597 quantity, it is important to acknowledge that this trend relies on the random samples  
598 being generally representative; a poorly chosen random set could still reduce  
599 generalizability. Notably, under both modes, the GBM-KNN-ERT method consistently  
600 exhibited significantly greater performance stability compared to the alternative  
601 ensemble, GBM4-KNN3. This enhanced robustness likely arises from its more

602 effective suppression of data heterogeneity and noise interference, indicating that more  
 603 complex ensemble methods possess a greater capacity to balance the benefits of  
 604 increased data quantity with the potential drawbacks of reduced data quality.



605  
 606 **Fig. 11. Performance comparison of two donor catchment selection methods for parameter**  
 607 **regionalization as a function of donor catchment quantity. Model (a-c) selects donor**  
 608 **catchments in order of decreasing NSE, while Mode 2 (d-f) selects them randomly. Flood**  
 609 **prediction accuracy is assessed using NSE, Qp, and Tp. Error bars represent the full range**  
 610 **(minimum to maximum) of the performance metrics.**

批注 [L22]: RC1, Comment #7

#### 611 5.4. The impact of climate change on parameter regionalization methods

612 The hydrological cycle within catchments is fundamentally governed by complex  
 613 interactions between climate and environmental factors. The Intergovernmental Panel  
 614 on Climate Change (IPCC) has consistently documented a continuous and accelerating  
 615 transition in global climatic patterns, characterized by increased variability and extreme  
 616 events (Pachauri et al., 2014). Consequently, future flood predictions derived from

617 parameter regionalization methods are expected to exhibit increased uncertainty and  
618 variability, highlighting the substantial influence of climate change on the reliability  
619 and precision of flood predictions in ungauged mountainous catchments (Yang et al.,  
620 2019). Therefore, a sensitivity analysis was designed to evaluate the robustness of the  
621 trained regionalization models when confronted with climatic conditions outside their  
622 original training range.

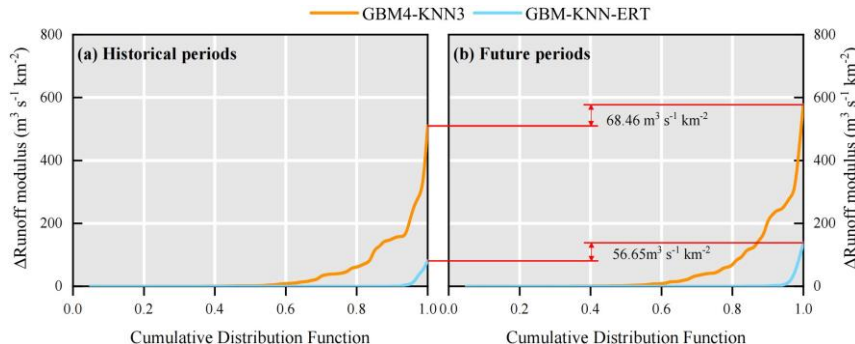
623 To quantitatively assess the impact of climate change, an experiment was devised  
624 where this impact was primarily reflected through changes in two key catchment  
625 descriptors: Tem and Pre. For the historical period, these descriptors represent the multi-  
626 year averages over 1901–2021, while for the future period, they represent the projected  
627 multi-year averages over 2022–2100 under the SSP5-8.5 scenario. The regionalization  
628 methods (GBM4-KNN3 and GBM-KNN-ERT), which were trained exclusively using  
629 historical data, were then applied under these future conditions. Crucially, the method  
630 structures and hyperparameters remained fixed, and no retraining was performed; only  
631 the historical Tem and Pre values were replaced with their future projections. This  
632 approach allows the response of the established historical relationships to new, out-of-  
633 sample climatic inputs to be tested. The simulated peak discharges for this analysis were  
634 derived from the same three flood events used in the calibration and validation of the  
635 Top-SSF model. This experimental design is critical as it isolates the impact of the  
636 changed model parameters from the compounding effect of a different future rainfall  
637 event. Consequently, any observed change in the simulated flood peak is attributable  
638 solely to the sensitivity of the regionalization method to the shift in climatic descriptors.

639 Cumulative distribution functions (CDFs) were then employed to illustrate the  
640 discrepancies between the parameter regionalization simulations and the reference  
641 simulations (derived from calibrated model parameters) across the historical and  
642 projected future periods for the 80 catchments (Fig.12).

643 A comparative analysis of Fig. 12a and 12b reveals a clear amplification of the  
644 absolute differences in predicted flood peaks (quantified as the error in runoff modulus)  
645 between the two parameter regionalization methods and the reference Top-SSF model  
646 simulations during the transition from the historical period to the projected future period.  
647 Specifically, the maximum error in runoff modulus for the GBM4-KNN3 method  
648 increased by  $68.46 \text{ m}^3 \text{ s}^{-1} \text{ km}^{-2}$  from the historical period to the future period, while the  
649 increase for the GBM-KNN-ERT method was a smaller  $56.65 \text{ m}^3 \text{ s}^{-1} \text{ km}^{-2}$ . These results  
650 underscore that parameter regionalization methods are inherently sensitive to changing  
651 climatic forcing. However, they also provide compelling evidence that the GBM-KNN-  
652 ERT method exhibits superior stability and resilience under climate change,  
653 demonstrating its potential for more reliable long-term flood risk assessment in  
654 ungauged mountainous regions.

655 Exploring the effects of climate change on parameter regionalization methods  
656 provides valuable insights for advancing flood prediction research in prediction in  
657 ungauged basins. The enhanced stability demonstrated by the GBM-KNN-ERT  
658 ensemble offers a promising direction for developing robust regionalization methods  
659 capable of navigating the challenges of a non-stationary climate.

批注 [L23]: RC1, Comment#8  
RC2 Comment#4



660  
661 **Fig.12.** Comparison of flood peak runoff modulus between parameter regionalization and  
662 calibrated Top-SSF model results, showing cumulative distribution functions (CDFs) of  
663 absolute differences for 80 catchments during (a) historical and (b) future periods.

### 664 5.5. Uncertainty and limitation

665 The uncertainty in this study arises from several sources, including the  
666 hydrological model, the regionalization methods, and the data itself. A critical  
667 evaluation of these sources helps to contextualize our findings and assess the  
668 generalizability of the ensemble method. Uncertainty from the hydrological model is  
669 inherent in its structure and the calibrated parameters. Although the Top-SSF model  
670 performed well, its parameters are effective values subject to equifinality. This  
671 uncertainty in the "true" parameter values can be viewed as a form of calibration bias,  
672 which serves as the target data for our regionalization. To mitigate this, we employed  
673 the robust SCE-UA optimization algorithm and focused only on sensitive parameters.  
674 Uncertainty is also introduced by the regionalization methods themselves, as the  
675 training data derived from donor catchments are susceptible to errors that can impact  
676 model performance (Mosavi et al., 2018; Xu et al., 2021).

677 A specific methodological choice was the exclusion of deep learning architectures,  
678 such as Multilayer Perceptrons or Long Short-Term Memory (LSTM) networks. This

679 decision was guided by several factors. First, parameter regionalization is a static  
680 regression problem, mapping time-invariant catchment descriptors to model parameters,  
681 which does not align with the sequential data structure for which LSTM is designed.  
682 Second, deep networks typically require large datasets to avoid overfitting; with a  
683 dataset of 80 catchments, traditional ML methods like GBM and ERT are often more  
684 robust and less prone to memorizing training data. Third, a key advantage of parameter  
685 regionalization over purely data-driven forecasting is its potential for physical  
686 interpretability. The tree-based models employed offer a degree of transparency,  
687 whereas DL models often function as "black boxes", a characteristic contrary to our  
688 goal of developing an interpretable tool for water resource management.

689 Furthermore, the primary contribution of this study is not the identification of a  
690 single superior algorithm, but the demonstration of a data-driven framework for  
691 constructing a locally optimal ensemble. The complementarity of the chosen models  
692 was not assumed but empirically validated through a competitive evaluation process.  
693 Each of the seven ML methods was independently trained and assessed for its ability to  
694 estimate each sensitive parameter. The final GBM-KNN-ERT ensemble was  
695 constructed by selecting only the empirically best-performing model for each parameter  
696 based on objective metrics ( $R^2$ , RMSE, STD). The very fact that different methods were  
697 selected for different hydrological parameters provides direct empirical evidence of  
698 their complementary strengths, thus validating the ensemble method.

699 Furthermore, the specific GBM-KNN-ERT combination identified is necessarily  
700 data-dependent, raising questions about its transferability. However, this study primary

701 contribution is not the specific model combination itself, but rather the demonstration  
702 of a data-driven method for constructing a locally optimal ensemble. This method is  
703 designed to be generalizable; applying the same competitive evaluation process to a  
704 new region would identify the best ensemble for that specific dataset. The key to  
705 overcoming these limitations and ensuring robust generalization lies in genuine model  
706 complementarity. The ensemble method's success is not an artifact of overfitting to  
707 calibration bias or data quirks. Instead, it stems from a physically plausible "division of  
708 labor," where different models are empirically shown to be better suited for  
709 regionalizing parameters governed by distinct physical processes. The ensemble  
710 method's superior stability in the out-of-sample climate change stress test further  
711 supports this conclusion, indicating that it has captured robust underlying relationships,  
712 not just noise.

713 To manage methodological uncertainty, we employed K-fold cross-validation to  
714 ensure robust performance evaluation and RandomizedSearchCV for hyperparameter  
715 tuning to minimize overfitting (Bergstra and Bengio, 2012). A key methodological  
716 decision was to evaluate the regionalization methods against the outputs of the  
717 calibrated Top-SSF model, rather than directly against observed flood events. This  
718 approach was chosen for two primary reasons. First, it isolates the performance of the  
719 parameter regionalization itself. The calibrated simulation represents the theoretical  
720 'best-case' performance for the given hydrological model structure; consequently, any  
721 deviation from this benchmark can be directly attributed to imperfections in the  
722 regionalization method, rather than being confounded by the inherent structural

723 limitations of the Top-SSF model. Second, this strategy ensures that the machine  
724 learning models learn the underlying physical relationships intended by the  
725 hydrological model, not simply mimic data noise or measurement errors present in the  
726 observations. If trained against raw observations, the ML methods might derive  
727 'spurious' parameter sets that compensate for both the hydrological model's structural  
728 flaws and observational errors. Such parameters could appear effective but would lack  
729 physical meaning and generalizability. These measures, combined with the evidence  
730 for model complementarity, provide a strong basis for the scientific validity and  
731 potential for generalization of our proposed ensemble method.

## 732 6. Conclusions

733 This study introduces a novel multi-machine learning ensemble method (GBM-  
734 KNN-ERT) to enhance model parameter transferability and improve flood prediction  
735 in ungauged mountainous catchments. The proposed GBM-KNN-ERT method  
736 demonstrated a substantial advancement in both flood prediction accuracy and model  
737 robustness, achieving exceptional performance with 90% of ungauged catchments  
738 exhibiting a NSE exceeding 0.9, a significant 67.44% improvement compared to the  
739 best single machine learning method evaluated in this study. Importantly, the GBM-  
740 KNN-ERT method exhibited remarkable stability under simulated climate change,  
741 thereby highlighting its potential for reliable application in non-stationary hydrological  
742 environments. Furthermore, the method demonstrated notable adaptability to varying  
743 donor-catchment configurations, where an optimal balance between predictive  
744 accuracy and computational efficiency with a relatively limited set of 20–40 high-

批注 [L24]: RC1, Comment#6

批注 [L25]: RC1, Comment#17

745 quality donor catchments (NSE >0.85). By integrating the diverse strengths of multiple  
746 machine learning with hydrological model, the proposed methodology significantly  
747 advances the field of flood prediction in ungauged catchments, offering a reliable tool  
748 for water resource management and flood disaster mitigation.

#### 749 **Acknowledgements**

750 This research was supported by the Joint Funds of the National Natural Science  
751 Foundation of China (**U2240226**), the National Natural Science Foundation of China  
752 (**42271038**) and the National Key Research and Development Program of China  
753 (**2022FY100205**).

#### 754 **Competing interests**

755 The authors declare that they have no known competing financial interests or  
756 personal relationships that could have appeared to influence the work reported in this  
757 paper.

#### 758 **Author contributions**

759 In this study, K L, G W, and J G were responsible for the conceptualization of the  
760 research. Data curation was carried out by K L, L G, and X S, while formal analysis  
761 was performed by K L, J G, and J M. The methodology was developed by K L, L G, P  
762 H, and J L. Project administration was overseen by G W and J G. K L took the lead in  
763 writing the original draft, and the writing, review, and editing process involved  
764 contributions from K L, G W, J L, P H, J M, X Z, and J G.

#### 765 **Code and data availability**

766 The code used in this study is available upon request from the authors. The

767 meteorological, soil characteristics, and topography datasets are publicly accessible  
768 online, as detailed in Table 1. The hourly flood data for the 80 catchments were sourced  
769 from China's Hydrological Yearbook. These data are not publicly available due to  
770 governmental restrictions but can be accessed by contacting the corresponding author  
771 for further information.

## 772 **References**

773 Arsenault, R., Breton-Dufour, M., Poulin, A., Dallaire, G.Romero-Lopez, R. (2019).  
774 Streamflow prediction in ungauged basins: analysis of regionalization methods  
775 in a hydrologically heterogeneous region of Mexico. *Hydrological Sciences  
776 Journal*, 64(11): 1297-1311. <https://doi.org/10.1080/02626667.2019.1639716>

777 Arsenault, R., Martel, J.Mai, J. (2022). Continuous streamflow prediction in ungauged  
778 basins: Long Short-Term Memory Neural Networks clearly outperform  
779 hydrological models. *Hydrol. Earth Syst. Sci.* 1-29.  
780 <https://doi.org/10.5194/hess-27-139-2023>

781 Bellman, R.E. (1961). On the reduction of dimensionality for classes of dynamic  
782 programming processes. RAND Corp., Santa Monica, Calif., Paper P-2243.

783 Bergstra, J.Bengio, Y. (2012). Random search for hyper-parameter optimization.  
784 *Journal of machine learning research*, 13(2).

785 Beven, K.J., Kirkby, M.J., Freer, J.E.Lamb, R. (2021). A history of TOPMODEL.  
786 *Hydrology and Earth System Sciences*, 25(2): 527-549.  
787 <https://doi.org/10.5194/hess-25-527-2021>

788 Bishop, C.M.Nasrabadi, N.M., (2006). Pattern recognition and machine learning  
789 (information science and statistics). New York: Springer - Verlag.

790 Breiman, L. (2001). Random forests. *Machine learning*, 45: 5-32.

791 Cheng, Q., Gao, L., Zuo, X.Zhong, F. (2019). Statistical analyses of spatial and  
792 temporal variabilities in total, daytime, and nighttime precipitation indices and  
793 of extreme dry/wet association with large-scale circulations of Southwest China,  
794 1961–2016. *Atmospheric research*, 219: 166-182.  
795 <https://doi.org/10.1109/ACCESS.2018.2886549>

796 Choi, J., Kim, U.Kim, S. (2023). Ecohydrologic model with satellite-based data for  
797 predicting streamflow in ungauged basins. *Science of The Total Environment*,  
798 903: 166617. <https://doi.org/10.1016/j.scitotenv.2023.166617>

799 Dai, Y., Shangguan, W., Duan, Q., Liu, B., Fu, S.Niu, G. (2013). Development of a  
800 China dataset of soil hydraulic parameters using pedotransfer functions for land  
801 surface modeling. *Journal of Hydrometeorology*, 14(3): 869-887.  
802 <https://doi.org/10.1175/JHM-D-12-0149.1>

803 Dakhlaoui, H., Bargaoui, Z.Bárdossy, A. (2012). Toward a more efficient calibration  
804 schema for HBV rainfall-runoff model. *Journal of Hydrology*, 444: 161-179.  
805 <https://doi.org/10.1016/j.jhydrol.2012.04.015>

806 Ding, Y.Peng, S. (2020). Spatiotemporal trends and attribution of drought across China  
807 from 1901–2100. *Sustainability*, 12(2): 477.  
808 <https://doi.org/10.3390/su12020477>

809 Duan, Q., Sorooshian, S.Gupta, V.K. (1994). Optimal use of the SCE-UA global  
810 optimization method for calibrating watershed models. *Journal of Hydrology*,  
811 158(3): 265-284. [https://doi.org/10.1016/0022-1694\(94\)90057-4](https://doi.org/10.1016/0022-1694(94)90057-4)

812 Friedman, J.H. (2002). Stochastic gradient boosting. *Computational statistics & data  
813 analysis*, 38(4): 367-378. [https://doi.org/10.1016/S0167-9473\(01\)00065-2](https://doi.org/10.1016/S0167-9473(01)00065-2)

814 Gan, B., Liu, X., Yang, X., Wang, X.Zhou, J. (2018). The impact of human activities on  
815 the occurrence of mountain flood hazards: lessons from the 17 August 2015  
816 flash flood/debris flow event in Xuyong County, south-western China.  
817 *Geomatics, Natural Hazards and Risk*, 9(1): 816-840.  
818 <https://doi.org/10.1080/19475705.2018.1480539>

819 Gao, J., Kirkby, M.Holden, J. (2018). The effect of interactions between rainfall  
820 patterns and land-cover change on flood peaks in upland peatlands. *Journal of  
821 Hydrology*, 567: 546-559. <https://doi.org/10.1016/j.jhydrol.2018.10.039>

822 Garambois, P.A., Roux, H., Larnier, K., Labat, D.Dartus, D. (2015). Parameter  
823 regionalization for a process-oriented distributed model dedicated to flash  
824 floods. *Journal of Hydrology*, 525: 383-399.  
825 <https://doi.org/10.1016/j.jhydrol.2015.03.052>

826 Gauch, M., Mai, J.Lin, J. (2021). The proper care and feeding of CAMELS: How  
827 limited training data affects streamflow prediction. *Environmental Modelling &  
828 Software*, 135: 104926. <https://doi.org/10.1016/j.envsoft.2020.104926>

829 Geurts, P., Ernst, D.Wehenkel, L. (2006). Extremely randomized trees. *Machine  
830 Learning*, 63(1): 3-42. <https://doi.org/10.1007/s10994-006-6226-1>

831 Golian, S., Murphy, C.Meresa, H. (2021). Regionalization of hydrological models for  
832 flow estimation in ungauged catchments in Ireland. *Journal of Hydrology:  
833 Regional Studies*, 36: 100859. <https://doi.org/10.1016/j.ejrh.2021.100859>

834 Guo, L., Huang, K., Wang, G.Lin, S. (2022). Development and evaluation of  
835 temperature-induced variable source area runoff generation model. *Journal of  
836 Hydrology*, 610: 127894. <https://doi.org/10.1016/j.jhydrol.2022.127894>

837 Guo, Y., Zhang, Y., Zhang, L.Wang, Z. (2021). Regionalization of hydrological  
838 modeling for predicting streamflow in ungauged catchments: A comprehensive  
839 review. *Wiley Interdisciplinary Reviews: Water*, 8(1): e1487.  
840 <https://doi.org/10.1002/wat2.1487>

841 Gupta, A.K., Chakraborty, S., Ghosh, S.K.Ganguly, S. (2023). A machine learning  
842 model for multi-class classification of quenched and partitioned steel  
843 microstructure type by the k-nearest neighbor algorithm. *Computational  
844 Materials Science*, 228: 112321.  
845 <https://doi.org/10.1016/j.commatsci.2023.112321>

846 Hastie, T., Tibshirani, R.Friedman, J., (2009). The elements of statistical learning.  
847 Citeseer.

848 Hersbach, H., Bell, B., Berrisford, P., Biavati, G., Horányi, A., Muñoz Sabater, J.,  
849 Nicolas, J., Peubey, C., Radu, R., Rozum, I., Schepers, D., Simmons, A., Soci,  
850 C., Dee, D.Thépaut, J.-N., (2023). ERA5 hourly data on single levels from 1940  
851 to present, Copernicus Climate Change Service (C3S) Climate Data Store  
852 (CDS)[Dataset]. <https://doi.org/10.24381/cds.adbb2d47> (Accessed on 08-06-  
853 2023)

854 Hua, F., Wang, L., Fisher, B., Zheng, X., Wang, X., Douglas, W.Y., Tang, Y., Zhu,  
855 J.Wilcove, D.S. (2018). Tree plantations displacing native forests: The nature  
856 and drivers of apparent forest recovery on former croplands in Southwestern  
857 China from 2000 to 2015. *Biological Conservation*, 222: 113-124.  
858 <https://doi.org/10.1016/j.biocon.2018.03.034>

859 Jordan, M.I.Mitchell, T.M. (2015). Machine learning: Trends, perspectives, and  
860 prospects. *Science*, 349(6245): 255-260. <https://doi.org/10.1126/science.aaa841>

861 Jung, Y. (2018). Multiple predicting K-fold cross-validation for model selection.  
862 *Journal of Nonparametric Statistics*, 30(1): 197-215.  
863 <https://doi.org/10.1080/10485252.2017.1404598>

864 Kanishka, G.Eldho, T. (2017). Watershed classification using isomap technique and  
865 hydrometeorological attributes. *Journal of Hydrologic Engineering*, 22(10):  
866 04017040. [https://doi.org/10.1061/\(ASCE\)HE.1943-5584.0001562](https://doi.org/10.1061/(ASCE)HE.1943-5584.0001562)

867 Kratzert, F., Klotz, D., Herrnegger, M., Sampson, A.K., Hochreiter, S.Nearing, G.S.  
868 (2019). Toward improved predictions in ungauged basins: Exploiting the power  
869 of machine learning. *Water Resources Research*, 55(12): 11344-11354.  
870 <https://doi.org/10.1029/2019WR026065>

871 Lenhart, T., Eckhardt, K., Fohrer, N.Frede, H.G. (2002). Comparison of two different  
872 approaches of sensitivity analysis. *Physics and Chemistry of the Earth, Parts*  
873 A/B/C, 27(9): 645-654. [https://doi.org/10.1016/S1474-7065\(02\)00049-9](https://doi.org/10.1016/S1474-7065(02)00049-9)

874 Li, K., Wang, G., Gao, J., Guo, L., Li, J.Guan, M. (2024). The rainfall threshold of  
875 forest cover for regulating extreme floods in mountainous catchments. *Catena*,  
876 236: 107707. <https://doi.org/10.1016/j.catena.2023.107707>

877 Li, X., Khandelwal, A., Jia, X., Cutler, K., Ghosh, R., Renganathan, A., Xu, S., Tayal,  
878 K., Nieber, J.Duffy, C. (2022). Regionalization in a global hydrologic deep  
879 learning model: from physical descriptors to random vectors. *Water Resources*  
880 *Research*, 58(8): e2021WR031794. <https://doi.org/10.1029/2021WR031794>

881 Li, Z., Xu, X., Yu, B., Xu, C., Liu, M.Wang, K. (2016). Quantifying the impacts of  
882 climate and human activities on water and sediment discharge in a karst region  
883 of southwest China. *Journal of Hydrology*, 542: 836-849.  
884 <https://doi.org/10.1016/j.jhydrol.2016.09.049>

885 Liu, C., Guo, L., Ye, L., Zhang, S., Zhao, Y.Song, T. (2018). A review of advances in  
886 China's flash flood early-warning system. *Natural hazards*, 92: 619-634.  
887 <https://doi.org/10.1007/s11069-018-3173-7>

888 Luo, P., He, B., Takara, K., Xiong, Y.E., Nover, D., Duan, W.Fukushi, K. (2015).  
889 Historical assessment of Chinese and Japanese flood management policies and

890        implications for managing future floods. *Environmental Science & Policy*, 48: 891        265-277. <https://doi.org/10.1016/j.envsci.2014.12.015>

892        McMillan, H.K. (2021). A review of hydrologic signatures and their applications. *Wiley 893        Interdisciplinary Reviews: Water*, 8(1): e1499. 894        <https://doi.org/10.1002/wat2.1499>

895        Morel-Seytoux, H.J.Khanji, J. (1974). Derivation of an equation of infiltration. *Water 896        Resources Research*, 10(4): 795-800. 897        <https://doi.org/10.1029/WR010i004p00795>

898        Mosavi, A., Ozturk, P.Chau, K.w. (2018). Flood prediction using machine learning 899        models: Literature review. *Water*, 10(11): 1536. 900        <https://doi.org/10.3390/w10111536>

901        Nearing, G., Cohen, D., Dube, V., Gauch, M., Gilon, O., Harrigan, S., Hassidim, A., 902        Klotz, D., Kratzert, F., Metzger, A., Nevo, S., Pappenberger, F., Prudhomme, C., 903        Shalev, G., Shenzis, S., Tekalign, T.Y., Weitzner, D.Matias, Y. (2024). Global 904        prediction of extreme floods in ungauged watersheds. *Nature*, 627(8004): 559- 905        563. <https://doi.org/10.1038/s41586-024-07145-1>

906        Pachauri, R.K., Allen, M.R., Barros, V.R., Broome, J., Cramer, W., Christ, R., Church, 907        J.A., Clarke, L., Dahe, Q.Dasgupta, P., (2014). Climate change 2014: synthesis 908        report. Contribution of Working Groups I, II and III to the fifth assessment 909        report of the Intergovernmental Panel on Climate Change.

910        Papageorgaki, I.Nalbantis, I. (2016). Classification of Drainage Basins Based on 911        Readily Available Information. *Water Resources Management*, 30(15): 5559- 912        5574. <https://doi.org/10.1007/s11269-016-1410-y>

913        Pugliese, A., Persiano, S., Bagli, S., Mazzoli, P., Parajka, J., Arheimer, B., Capell, R., 914        Montanari, A., Blöschl, G.Castellarin, A. (2018). A geostatistical data- 915        assimilation technique for enhancing macro-scale rainfall-runoff simulations. 916        *Hydrology and Earth System Sciences*, 22(9): 4633-4648. 917        <https://doi.org/10.5194/hess-22-4633-2018>

918        Qi, W., Zhang, C., Fu, G.Zhou, H. (2016). Quantifying dynamic sensitivity of 919        optimization algorithm parameters to improve hydrological model calibration. 920        *Journal of Hydrology*, 533: 213-223. 921        <https://doi.org/10.1016/j.jhydrol.2015.11.052>

922        Ragettli, S., Zhou, J., Wang, H., Liu, C.Guo, L. (2017). Modeling flash floods in 923        ungauged mountain catchments of China: A decision tree learning approach for 924        parameter regionalization. *Journal of Hydrology*, 555: 330-346. 925        <https://doi.org/10.1016/j.jhydrol.2017.10.031>

926        Rockström, J., Gupta, J., Qin, D., Lade, S.J., Abrams, J.F., Andersen, L.S., Armstrong 927        McKay, D.I., Bai, X., Bala, G., Bunn, S.E., Ciobanu, D., DeClerck, F., Ebi, K., 928        Gifford, L., Gordon, C., Hasan, S., Kanie, N., Lenton, T.M., Loriani, S., 929        Liverman, D.M., Mohamed, A., Nakicenovic, N., Obura, D., Ospina, D., 930        Prodani, K., Rammelt, C., Sakschewski, B., Scholtens, J., Stewart-Koster, B., 931        Tharammal, T., van Vuuren, D., Verburg, P.H., Winkelmann, R., Zimm, C., 932        Bennett, E.M., Bringezu, S., Broadgate, W., Green, P.A., Huang, L., Jacobson, 933        L., Ndehedehe, C., Pedde, S., Rocha, J., Scheffer, M., Schulte-Uebbing, L., de

934 Vries, W., Xiao, C., Xu, C., Xu, X., Zafra-Calvo, N.Zhang, X. (2023). Safe and  
935 just Earth system boundaries. *Nature*, 619(7968): 102-111.  
936 <https://doi.org/10.1038/s41586-023-06083-8>

937 Sain, S.R. (1996). The Nature of Statistical Learning Theory. *Technometrics*, 38(4):  
938 409-409. <https://doi.org/10.1080/00401706.1996.10484565>

939 Salmeron, R., García, C.García, J. (2018). Variance inflation factor and condition  
940 number in multiple linear regression. *Journal of statistical computation and*  
941 *simulation*, 88(12): 2365-2384.  
942 <https://doi.org/10.1080/00949655.2018.1463376>

943 Schoups, G., van de Giesen, N.C.Savenije, H.H.G. (2008). Model complexity control  
944 for hydrologic prediction. *Water Resources Research*, 44(12).  
945 <https://doi.org/10.1029/2008WR006836>

946 Shangguan, W., Dai, Y., Liu, B., Zhu, A., Duan, Q., Wu, L., Ji, D., Ye, A., Yuan,  
947 H.Zhang, Q. (2013). A China data set of soil properties for land surface  
948 modeling. *Journal of Advances in Modeling Earth Systems*, 5(2): 212-224.  
949 <https://doi.org/10.1002/jame.20026>

950 Song, Z., Xia, J., Wang, G., She, D., Hu, C.Hong, S. (2022). Regionalization of  
951 hydrological model parameters using gradient boosting machine. *Hydrology*  
952 and *Earth System Sciences*, 26(2): 505-524. <https://doi.org/10.5194/hess-26-505-2022>

954 Tang, S., Sun, F., Liu, W., Wang, H., Feng, Y.Li, Z. (2023). Optimal Postprocessing  
955 Strategies With LSTM for Global Streamflow Prediction in Ungauged Basins.  
956 *Water Resources Research*, 59(7): e2022WR034352.  
957 <https://doi.org/10.1029/2022WR034352>

958 Wainwright, J.Mulligan, M., (2013). Environmental modelling: finding simplicity in  
959 complexity. John Wiley & Sons.

960 Wani, O., Beckers, J.V.L., Weerts, A.H.Solomatine, D.P. (2017). Residual uncertainty  
961 estimation using instance-based learning with applications to hydrologic  
962 forecasting. *Hydrol. Earth Syst. Sci.*, 21(8): 4021-4036.  
963 <https://doi.org/10.5194/hess-21-4021-2017>

964 Wu, H., Zhang, J., Bao, Z., Wang, G., Wang, W., Yang, Y.Wang, J. (2022). Runoff  
965 modeling in ungauged catchments using machine learning algorithm-based  
966 model parameters regionalization methodology. *Engineering*.  
967 <https://doi.org/10.1016/j.eng.2021.12.014>

968 Xu, Q., Chen, J., Peart, M.R., Ng, C.-N., Hau, B.C.H.Law, W.W.Y. (2018). Exploration  
969 of severities of rainfall and runoff extremes in ungauged catchments: A case  
970 study of Lai Chi Wo in Hong Kong, China. *Science of The Total Environment*,  
971 634: 640-649. <https://doi.org/10.1016/j.scitotenv.2018.04.024>

972 Xu, T.Liang, F. (2021). Machine learning for hydrologic sciences: An introductory  
973 overview. *Wiley Interdisciplinary Reviews: Water*, 8(5).  
974 <https://doi.org/10.1002/wat2.1533>

975 Yang, X., Magnusson, J., Rizzi, J.Xu, C.-Y. (2018). Runoff prediction in ungauged  
976 catchments in Norway: comparison of regionalization approaches. *Hydrology*  
977 *Research*, 49(2): 487-505. <https://doi.org/10.2166/nh.2017.071>

978 Yang, X., Magnusson, J.Xu, C.Y. (2019). Transferability of regionalization methods  
979 under changing climate. *Journal of Hydrology*, 568: 67-81.  
980 <https://doi.org/10.1016/j.jhydrol.2018.10.030>

981 Zhai, X., Guo, L., Liu, R.Zhang, Y. (2018). Rainfall threshold determination for flash  
982 flood warning in mountainous catchments with consideration of antecedent soil  
983 moisture and rainfall pattern. *Natural Hazards*, 94: 605-625.  
984 <https://doi.org/10.1007/s11069-018-3404-y>

985 Zhang, B., Ouyang, C., Cui, P., Xu, Q., Wang, D., Zhang, F., Li, Z., Fan, L., Lovati, M.,  
986 Liu, Y.Zhang, Q. (2024). Deep learning for cross-region streamflow and flood  
987 forecasting at a global scale. *The Innovation*, 5(3).  
988 <https://doi.org/10.1016/j.xinn.2024.100617>

989 Zhang, Y., Chiew, F.H., Li, M.Post, D. (2018). Predicting runoff signatures using  
990 regression and hydrological modeling approaches. *Water Resources Research*,  
991 54(10): 7859-7878. <https://doi.org/10.1029/2018WR023325>

992 Zhang, Y., Chiew, F.H., Liu, C., Tang, Q., Xia, J., Tian, J., Kong, D.Li, C. (2020). Can  
993 remotely sensed actual evapotranspiration facilitate hydrological prediction in  
994 ungauged regions without runoff calibration? *Water Resources Research*, 56(1):  
995 e2019WR026236. <https://doi.org/10.1029/2019WR026236>

996 Zhang, Y., Ragettli, S., Molnar, P., Fink, O.Peleg, N. (2022). Generalization of an  
997 Encoder-Decoder LSTM model for flood prediction in ungauged catchments.  
998 *Journal of Hydrology*, 614: 128577.  
999 <https://doi.org/10.1016/j.jhydrol.2022.128577>

1000 Zounemat-Kermani, M., Batelaan, O., Fadaee, M.Hinkelmann, R. (2021). Ensemble  
1001 machine learning paradigms in hydrology: A review. *Journal of Hydrology*, 598:  
1002 126266. <https://doi.org/10.1016/j.jhydrol.2021.126266>

1003